

# A COMPUTATIONAL AND EXPERIMENTAL ANALYSIS OF A DUCTED FAN USED IN VTOL UAV SYSTEMS

*Ali Akturk<sup>1</sup> and Cengiz Camci<sup>2</sup>*

Turbomachinery Aero-Heat Transfer Laboratory  
Department Aerospace Engineering  
Pennsylvania State University  
University Park, PA 16802

## ABSTRACT

Ducted fan based vertical/short take-off and landing (VTOL) uninhabited aerial vehicles (UAV) are frequently used because they offer higher disk loading compared to open rotors and improve propulsive performance. A three-dimensional RANS based computational analysis is implemented for high resolution analysis of these systems under realistic operational conditions. Fan rotor field including secondary flows, tip vortices, blade boundary layers and the wake system is simulated for hover conditions. RANS prediction of hover performance was compared to available wind tunnel test data. Total pressure measurements and computational predictions of mean flow at the fan rotor exit are in very good agreement at hover conditions. The measured and simulated rotor exit field shows a significant level of 3D hub separation affecting the overall performance of the ducted fan. Edgewise flight predictions for the specific ducted fan are in progress.

## NOMENCLATURE

$\beta_1$	Blade section inlet angle (deg)
$\beta_2$	Blade section exit angle (deg)
$c$	Chord length (m)
$D$	Overall diameter of the baseline ducted fan (m)
$P_a$	Atmospheric pressure (pa)
$P_T$	Total pressure (pa)
$\rho$	Density (kg/m <sup>3</sup> )
$\Omega$	Rotational speed (radian/s)
$r$	Radial distance measured from origin (m)
$R_{tip}$	Rotor tip radius (m)
$\Re$	Ideal gas constant,(for air $\Re=287$ J/Kg.K)
$T_a$	Atmospheric temperature (K)

## INTRODUCTION

Military uninhabited air vehicle developers have a great interest in ducted fan Vertical Take off and Landing (VTOL) Unmanned Aerial Vehicles (UAVs). In addition to conventional military tasks, they can continuously transmit surveillance data and act as a relay station. Although ducted fans may provide high performance in many VTOL applications, there are still unresolved problems associated with them especially in the forward flight mode. Although early full scale ducted fan based air vehicles such as Bell X-22A and DOAK VZ-4 (Mort and Yaggy (1962; 1961)) provided a significant amount of information and operational data, the ducted fan performance issues related to inlet lip separation and tip clearance problems still contribute to the performance issues in present day systems.

Experimental investigation has been one of the major approaches to study the flow characteristics of ducted fans. Abrego and Bulaga (2002) performed wind tunnel tests to determine the performance characteristics of ducted fans for axial and edgewise flight conditions. Fleming *et al.*(2004) conducted

---

<sup>1</sup>Postdoctoral Research Fellow, e-mail: aua162@psu.edu

<sup>2</sup>Professor of Aerospace Engineering, corresponding author, e-mail: cxc11@psu.edu

wind tunnel experiments and computational studies around a 305 mm diameter ducted fan. They have concentrated on the performance of ducted fan VTOL vehicles in crosswind.

Graf *et al.* (2008) improved ducted fan forward flight performance using a newly designed leading edge geometry which has been determined to be the significant factor in offsetting the effects of the adverse aerodynamic characteristics.

Akturk, Shavalikul and Camci (2009) experimentally investigated the complicated flow field around the ducted fan in hover and forward flight conditions. Flow features such as inlet lip separation, distortion of inlet flow features before and after the axial fan rotor, influence of rotor tip speed, influence of forward flight velocity and the interaction of the cross wind with fan exit jet were investigated through planar particle image velocimetry (PIV) experiments. A three dimensional viscous flow computation of the specific ducted fan system was also presented.

Mort and Yaggy (1962; 1961) performed hover and forward flight tests on a 1.22 m diameter wing tip mounted ducted fan that is used on Doak VZ-4-DA. Performance characteristics for the ducted fan were reported.

Mort and Gamse (1967) investigated aerodynamic characteristics of a 2.13 m diameter ducted propeller which was used on the Bell Aerosystems Co. X-22A airplane. Stall of both the upstream and downstream duct lips of this 2.13 m diameter ducted fan was examined in function of angle of attack. It was found that the onset of separation on the upstream lip will be encountered; however, complete separation on this lip will be encountered only during conditions of low power and high duct angle of attack.

Akturk and Camci (2010) performed an experimental study using total pressure measurements at the exit of the fan rotor to investigate effect of tip leakage flow in hover and forward flight condition. Complex tip leakage flow and low momentum re-circulatory flow from the inlet lip separation area strongly interact with the rotor passage flow. Measurements were obtained at various circumferential positions so that the inlet flow distortion effect on rotor performance was investigated.

In addition to experimental studies, the ducted fan design and performance analyses were widely performed by using computational methods. Lind *et al.* (2006) carried out a computational study using a panel method to compare their results to the experimental results from Martin and Tung (2004). He and Xin (2006) developed ducted fan models based on a non-uniform and unsteady ring vortex formulation. A numerical study in axial and horizontal flight conditions was conducted and validated with measured data. Chang *et al.* (2003) developed an accurate grid generation methodology known as “*the curve adaptive option*” to model several industrial ducted fans. Their computational results agreed well with available wind tunnel data. Ahn *et al.* (2004) applied a computational method to their ducted fan system to identify the design parameters which affect its performance. Their ducted fan system was designed by using the stream-surface based axisymmetric analysis. Ko *et al.* (2007) developed a computer code aimed at the preliminary design of a ducted fan system. This code was validated using data from many wind tunnel and flight tests. It was also extensively used in the design of commercial ducted fans. Recently, Zhao and Bil (2008) proposed a CFD simulation to design and analyze an aerodynamic model of a ducted fan UAV in preliminary design phase with different speeds and angles of attacks.

The current computational study uses simulations of incompressible mean flow field around the ducted fan where the fan rotor tip mach number is 0.228 for which the compressibility effects are not significant. The simulations were performed using general purpose code Ansys-CFX (2009b; 2009a). The implementation of the specific computational method is outlined in following sections. Predictions for hover performance for 127 mm diameter ducted fan were compared to available wind tunnel data. The motivation of this study is to develop implementations of computational algorithms for the fans that use full rotor simulations. One of the main goals is to understand the sources of the aerodynamic losses generated at the fan rotor exit flow field.

## COMPUTATIONAL MODEL DESCRIPTION

Three dimensional computational methods can be used for analyzing viscous and turbulent flow field around and inside the ducted fan for hover and forward flight conditions. High resolution total pressure results experimentally obtained in this study constitute a good set of data for validation of computational algorithms. A simulation of the incompressible mean flow field around the ducted fan

was performed using general purpose code Ansys-CFX (2009b; 2009a). The specific computational system solves the Reynolds-Averaged Navier-Stokes equations using an element based finite volume method in the ducted fan rotor and around the ducted fan driven VTOL UAV. The mass, momentum and energy equations are simultaneously solved over an unstructured finite volume based mesh system.

### Discretization of Governing Equations

Governing equations that provide a complete mathematical description of the fluid flow are conservation of mass, momentum and a passive scalar expressed in scalar coordinates in equations 1, 2, 3

$$\frac{\partial \rho}{\partial t} + \frac{\partial}{\partial x_j} (\rho U_j) = 0.0 \quad (1)$$

$$\frac{\partial}{\partial t} (\rho U_j) + \frac{\partial}{\partial x_j} (\rho U_j U_i) = -\frac{\partial P}{\partial x_i} + \frac{\partial}{\partial x_j} \left( \mu_{eff} \left( \frac{\partial U_i}{\partial x_j} + \frac{\partial U_j}{\partial x_i} \right) + S_{U_i} \right) \quad (2)$$

$$\frac{\partial}{\partial t} (\rho \phi) + \frac{\partial}{\partial x_j} (\rho U_j \phi) = \frac{\partial}{\partial x_j} \left( \Gamma_{eff} \left( \frac{\partial \phi}{\partial x_j} \right) \right) + S_\phi \quad (3)$$

The equations 1, 2 and 3 are integrated over control volume. Volume integrals involving divergence and gradient operators are converted to the surface integrals using Gauss' Divergence Theorem, and equations 4, 5 and 6 are obtained. Equation 3 is usually used in the simulation of energy equation for temperature distribution over the domain.

$$\frac{d}{dt} \int_V \rho dV + \int_S \rho U_j dn_j = 0.0 \quad (4)$$

$$\frac{d}{dt} \int_V \rho U_i dV + \int_S \rho U_j U_i dn_j = \int_S P dn_j + \int_S \mu_{eff} \left( \frac{\partial U_i}{\partial x_j} + \frac{\partial U_j}{\partial x_i} \right) dn_j + \int_V S_{U_i} dV \quad (5)$$

$$\frac{d}{dt} \int_V \rho \phi dV + \int_S \rho U_j \phi dn_j = \int_S \Gamma_{eff} \left( \frac{\partial \phi}{\partial x_j} \right) dn_j + \int_V S_\phi dV \quad (6)$$

V and S in the equations 4, 5 and 6 respectively denote volume and surface regions of integration, and  $dn_j$  are the Cartesian components of the outward normal surface vector. The volume and surface integrals in this section are discretized by using an unstructured mesh. Volume integrals are discretized within each element sector and accumulated to the control volume to which the sector belongs. Surface integrals are discretized at the integration points (ipn) located at the center of each surface segment within an element and then distributed to the adjacent control volumes. Because the surface integrals are equal and opposite for control volumes adjacent to the integration points, the surface integrals are guaranteed to be locally conservative. ANSYS CFX uses second order accurate approximations Ansys-CFX (2009b; 2009a).

### Turbulence Model

K- $\omega$  based shear stress transport model used for computations in this paper. K- $\omega$  turbulence model was developed by Wilcox (1993). It solves two transport equations, one for the turbulent kinetic energy and one for the turbulent frequency,  $\omega$ . The stress tensor is computed from the eddy viscosity concept.

**k-equation:**

$$\frac{\partial \rho k}{\partial t} + \nabla \cdot (\rho U k) = \nabla \cdot \left[ \left( \mu + \frac{\mu_t}{\sigma_k} \right) \nabla k \right] + P_k + P_{kb} - \beta' \rho k \omega \quad (7)$$

**$\omega$ -equation:**

$$\frac{\partial \rho \omega}{\partial t} + \nabla \cdot (\rho U \omega) = \nabla \cdot \left[ \left( \mu + \frac{\mu_t}{\sigma_\omega} \right) \nabla \omega \right] + P_\omega + P_{\omega b} - \beta \rho \omega^2 \quad (8)$$

Beside the independent variables, the density,  $\rho$ , and the velocity vector, U, are treated as known quantities from the Navier-Stokes method.  $P_k$  is the production rate of turbulence, which is calculated

as:

$$P_k = \mu_t \nabla U \cdot (\nabla U + \nabla U^T) - \frac{2}{3} \nabla \cdot U (3\mu_t \nabla \cdot U + \rho k) \quad (9)$$

The  $k-\omega$  based shear stress transport model is used in our computations. This model accounts for the transport of the turbulent shear stress and gives accurate predictions of the flow separation under adverse pressure gradient. The proper transport behavior can be obtained by a limiter to the formulation of the eddy-viscosity:

The model constants are given by :

$$\begin{aligned} \beta' &= 0.09 \\ \alpha &= 5/9 \\ \beta &= 0.075 \\ \sigma_k &= 2 \\ \sigma_\omega &= 2 \\ a_1 &= 0.31 \end{aligned} \quad (10)$$

$$\mu_t = \frac{\rho a_1 k}{\max(a_1 \omega, S F_2)} \quad (11)$$

where  $F_2$  is a blending function, which restricts the limiter to the wall boundary layer, as the underlying assumptions are not correct for free shear flows.  $S$  is an invariant measure of the strain rate.

$$F_2 = \tanh \left( \max \left[ \frac{2\sqrt{k}}{\beta' \omega y}, \frac{500\nu}{y^2 \omega} \right]^2 \right) \quad (12)$$

where  $y$  is the distance to the nearest wall,  $\nu$  is the kinematic viscosity and the magnitude of strain rate,  $S$ , is given as :

$$S = \frac{1}{2} \left( \frac{\partial U_i}{\partial x_j} + \frac{\partial U_j}{\partial x_i} \right) \quad (13)$$

### Rotational Forces

For simulating flow in a rotating frame of reference, rotating at a constant angular velocity  $\Omega$ , additional sources of momentum are required to account for the effects of the Coriolis force and the centrifugal force (Ansys-CFX (2009b; 2009a)). The source terms in equation 2 and 3 are modified as:

$$S_{M,rot} = S_{Cor} + S_{cfg} \quad (14)$$

where:

$$S_{Cor} = -2\rho\Omega \times U \quad (15)$$

$$S_{cfg} = -\rho\Omega \times (\Omega \times r) \quad (16)$$

and where  $r$  is the location vector and  $U$  is the relative frame velocity (that is, the rotating frame velocity for a rotating frame of reference)(Ansys-CFX (2009b; 2009a)).

### Boundary Conditions for Hover

For the simulation of the ducted fan in hover condition, the computational domain is divided into two stationary (inlet and outlet regions) and one rotational frames (rotating fan blades). Figure 1 shows stationary and rotational frames. Inlet lip region includes an inlet lip surface that is considered as solid wall with no-slip condition. Atmospheric static pressure is prescribed on the top surface. On the side surface, opening boundary condition is assumed. An opening boundary condition allows the fluid to cross the boundary surface in either direction. For example, all of the fluid might flow into the domain at the opening, or all of the fluid might flow out of the domain, or a mixture of the two might occur. (Ansys-CFX (2009b; 2009a)).

The outlet region includes outlet guide vanes, tailcone surface, duct inner surface and duct outer surface that are considered as solid walls with no-slip condition. Atmospheric static pressure is prescribed on the bottom surface. On the side surface, an opening boundary condition is assumed.

The rotating region includes fan blades, rotor hub region and shroud surface. The rotating fluid

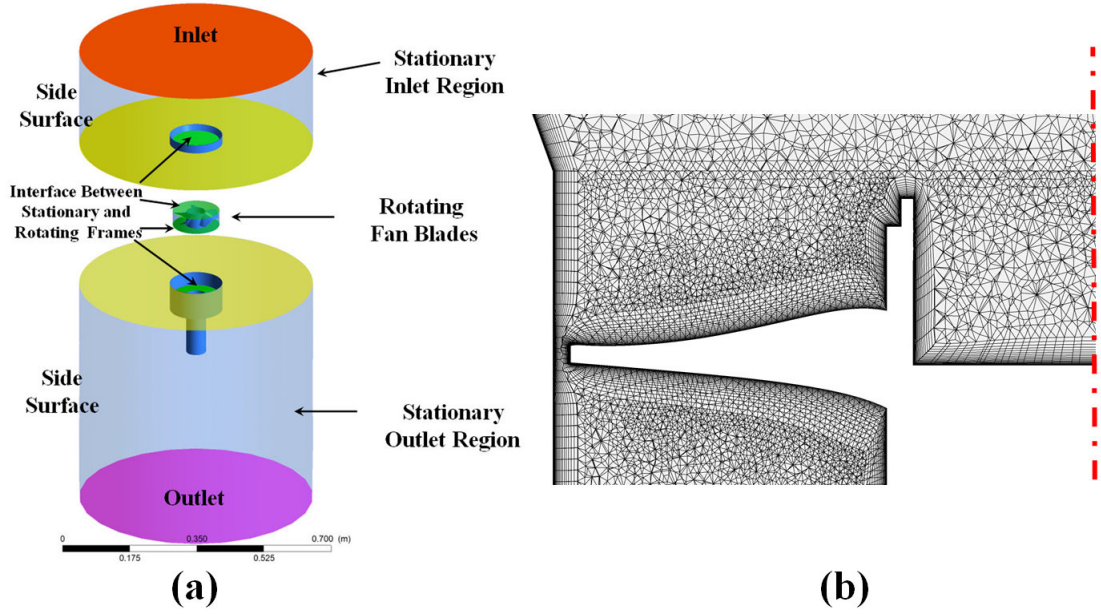


Figure 1: (a) Computational domain and boundary conditions for hover condition (b) Medium size computational mesh used in computations

motion is simulated by adding source terms for Coriolis forces and centrifugal forces. Counter rotating wall velocities are assigned at the shroud surface.

#### *Interfaces Between Rotating and Stationary Frames*

When one side is in a stationary frame and the other side is in a rotating frame of reference, interface should be used for connection. A “Stage” type interface model is used in calculations for modeling the frame change. The stage model performs a circumferential averaging of the fluxes on the interface. One-time mixing loss which is equivalent to assume that the physical mixing supplied by the relative motion between rotating and stationary components is introduced by circumferential averaging. The inlet and outlet stationary frames are connected using an interface that provides general connection without frame change. General grid interface (GGI) is used for mesh connections between interfaces (Ansys-CFX (2009b; 2009a)). GGI connections refer to the grid connections where the grid on either side of the two connected interface surfaces does not match.

### EXPERIMENTAL DATA

Experimental measurements (Akturk and Camci (2010)) were performed on a custom designed and fabricated 127 mm diameter ducted fan test system in the Penn State mid-sized wind tunnel for hover and forward flight conditions. Absolute total pressure measurements were obtained at the 10 mm downstream of the five-bladed fan rotor measured from midspan. Thrust measurements were also performed using a uni-axial load cell mounted underneath of the ducted fan test system.

The experimental uncertainties were defined in Akturk and Camci ((2010)). The total pressure measurement uncertainty was estimated as  $\pm 8$  Pa that is originating from the Kiel probe head, the pneumatic circuit, pressure transducer, local Re number magnitude and turbulence intensity. The uncertainty in thrust measurements was given as  $\pm 0.041$  N.

#### **Ducted Fan Model**

The computational method described earlier was applied to simulate the 127 mm diameter ducted fan shown in Figure 2 for the hover condition. The brushless DC electric motor driving the five bladed ducted fan rotor is speed controlled by a Castle HV-110 electronic speed control (ESC) system. The

high efficiency Neu 1521/1.5Y electric motor driving the fan can deliver 1.5 KW power. The ducted fan provides a disk loading range from 240 to 1676 Pa in a corresponding rotor speed range from 5000 rpm to 20,000 rpm.

Figure 2 shows the five bladed ducted fan rotor that is used in the present computational study. The main geometric parameters of the rotor system are presented in Table 1. This ducted fan unit manufactured from carbon composite material is designed for small scale uninhabited air vehicles. Six outlet guide vanes (OGV) remove some of the swirl at the exit of the rotor. The OGVs also cancel some of the torque acting on the vehicle. A tail cone is used to cover the motor surface and hide the electrical wiring for the wind tunnel model. An optical once-per-revolution device located near the hub of the rotor exit is used for the measurement of rotational speed of the fan rotor.

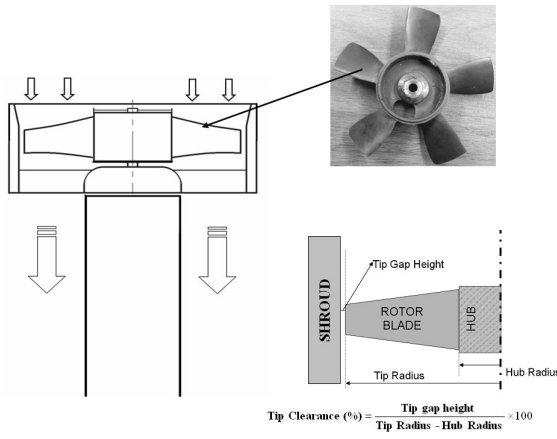


Figure 2: Ducted fan, five-bladed fan rotor and tip clearance definition

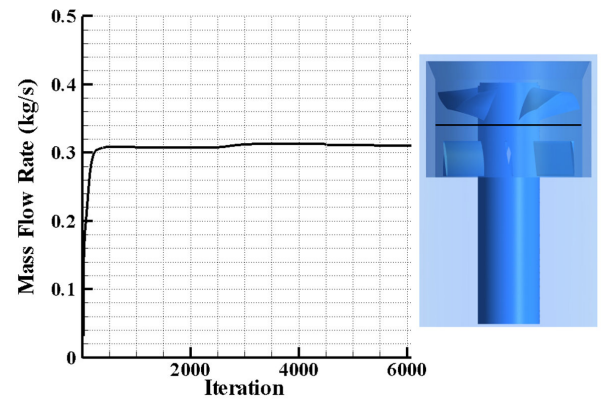


Figure 3: Convergence history plot of mass flow rate at the downstream of fan rotor

		Rotor blade section properties		
	Metric	Hub	Mid Span	Tip
Rotor hub diameter	52 mm	60°	40°	30°
Rotor tip diameter	120 mm	30°	45°	60°
Rotor blade span	34 mm	32 mm	30 mm	28 mm
Max. blade thickness @ tip	1.5 mm			
Shroud inner diameter for %5.8 tip clearance	122.9 mm			

Table 1: Geometric specifications of 127 mm ducted fan

The ducted fan system was supported by a steel support shaft connected to the the center of the tailcone. The steel support shaft was held in place by two low friction linear bearings to minimize friction while effectively isolating only the thrust associated with the ducted fan system.

## COMPUTATIONAL PROCEDURE

The computational results are obtained at 12000 rpm for hover condition. Calculations are performed using a parallel processing approach. For the parallel processing approach, stationary and rotating frames are partitioned via vertex based partitioning with metis multilevel k-way algorithm (Ansys-CFX (2009b; 2009a)). Computations are performed using 24 processors. Total processing time is approximately 48.5 hours. Steady state solutions are obtained after approximately 6000 iterations. Figure 3 shows the convergence history plot of mass flow rate downstream of the fan rotor.

### Computational Grid

Unstructured tetrahedral cells are used for the current computations. Regions near the solid surfaces are meshed with prisms for generating the viscous boundary layer grid. Non-dimensional wall

distance ( $y^+$ ) less than 2 is achieved near the casing and hub region. The region between solid casing and rotating blade tips is filled with prism layers.

#### Grid Refinement Study

A grid independence study is performed to show that the computational results are not dependent on the computational mesh characteristics and that the resolution of the mesh is adequate to capture the significant flow characteristics. The grid independence is evaluated by comparing the computational solutions from 3 different mesh sizes, comprising coarse mesh with 3,350,000 tetrahedral cells, medium mesh with 4,500,000 cells and 5,000,000 cells. The static pressure distribution around the midspan blade profile is plotted in Figure 4 for these different grid densities. The profile suggests that the computational results are grid independent when the 4,500,000 cells are exceeded.

The fan rotor exit total pressure measurements are also compared for three mesh sizes at midspan. The computations obtained with coarse mesh predicts fan rotor exit total pressure 8.8 % of rotor inlet dynamic head higher than medium mesh. When medium and fine mesh sizes are compared, the difference in fan rotor exit total pressure is 1.2 % of rotor inlet dynamic head, corresponding to  $\pm 2.5$  Pa. This value is well below the estimated total pressure measurement accuracy. Therefore, the medium mesh is used for all predictions in this paper.

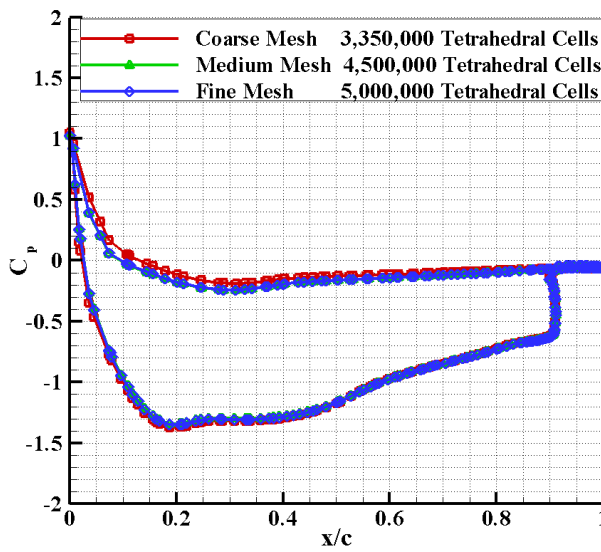


Figure 4: Grid independency study

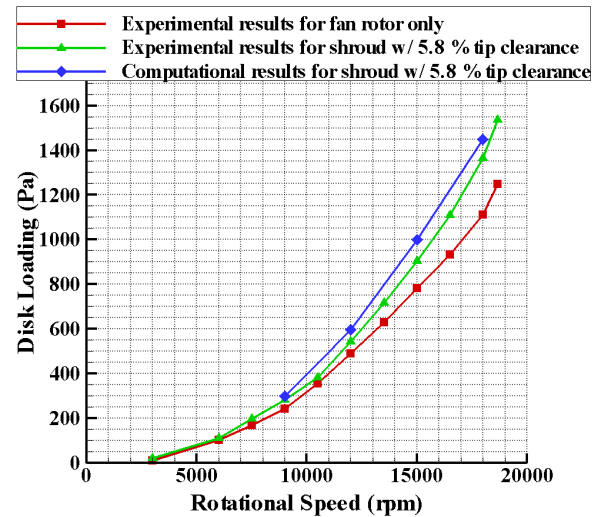


Figure 5: Computed and measured disk loading versus rotational speed at hover condition  
Measurement uncertainty =  $\pm 3.16$  Pa

## VALIDATION OF NUMERICAL RESULTS

### Disk loading comparison

Thrust measurements were obtained at hover condition for various rotor speeds. Thrust measurements are normalized in the form of disk loading, which is thrust force per unit rotor disk area. The disk loading parameter is a significant indicator of how a rotor disk is fluid mechanically loaded as a result of a complex energy addition process to air in a fan rotor passage. The flow quality in a fan rotor passage is directly controlled by the adverse pressure gradients and highly re-circulatory/turbulent flow conditions, in a rotating frame of reference.

Computed and measured disk loadings are compared in Figure 5. Figure 5 shows that adding a shroud to the fan system increases the thrust leading to improved rotor disk loading. The disk loading predictions agreed well for low rotational speeds. However, the relative error slightly increased while rotational speed was increased because the compressibility effect is more significant for the high ro-



tational speeds.

### Exit total pressure comparison

Figure 6 shows comparison of experimental and computational results obtained for the 127 mm diameter ducted fan. In this steady state rotor computation, circumferentially area averaged total pressure values computed at the 10mm downstream of the fan rotor are compared to the experimental results. Total pressure results were expressed in non-dimensional form as a total pressure coefficient throughout this paper.

$$C_{pTotal} = \frac{P_t - P_a}{\frac{1}{2}\rho V_{ref}^2} \text{ where } \rho = \frac{P_a}{RT_a} \quad (17)$$

The reference velocity used in equation 17 was calculated from the fan rotor tip speed.

$$V_{ref} = \Omega \times R_{tip} \quad (18)$$

All the radial coordinates are given in non-dimensional form ( $\frac{r}{R_{tip}}$ ) throughout this study.

The computational and experimental results show very good agreement in the spanwise distribution except in a limited area near the hub where  $r/R_{tip} \leq 0.6$ . The computational results somewhat deviate from experimental results near the hub region. That is because of the highly complex low Reynolds number, separated turbulent flow field near the hub region. A combination of high rotational speed and low Reynolds number characteristic of the flow makes this computation highly challenging. A highly 3D and separated hub endwall flow system exists in this area.

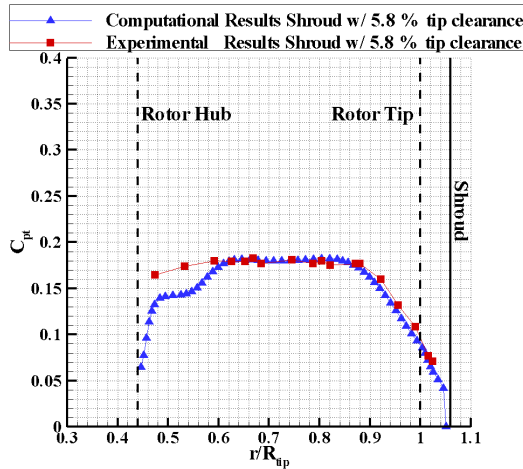


Figure 6: Comparison of experimental results to computational predictions at hover condition at 12000 rpm (10 mm downstream of the fan rotor measured from midspan )  
Measurement uncertainty =  $\pm 8$  Pa

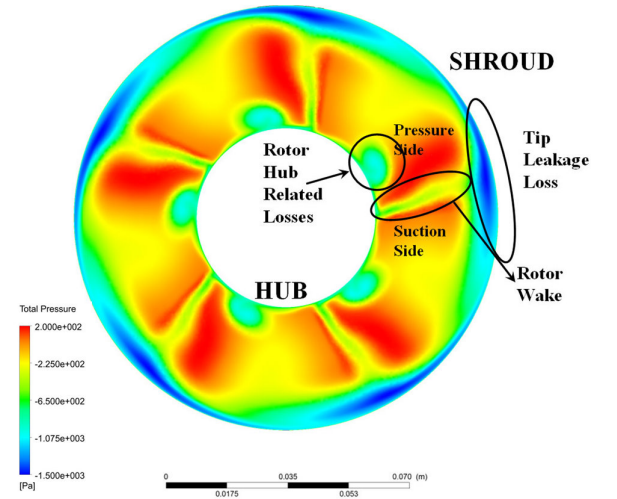


Figure 7: Fan rotor exit relative total pressure contour

### HOVER CONDITION RESULTS AND FLOW FIELD AROUND THE FAN ROTOR

Figure 7 shows relative total pressure distribution drawn downstream of the fan rotor at 12000 rpm in relative frame. Contour plot is drawn on the plane that is tangent to the blade trailing edge at the rotor hub. Gains and losses in the flow field due to rotating fan rotor can be seen from the Figure. Red regions show high total pressure regions where rotor blade added energy to the flow whereas light and dark blue regions show low momentum fluid regions where energy of the flow is dissipated by aerodynamic losses. Losses generated from fan rotor blade surfaces are marked as “rotor wake



*losses*” in the contour plot. Tip leakage losses are generated near the shroud. Leakage flow from the suction side to the pressure side generates significant amount of loss in the rotor exit flow field. It is obvious from the Figure that tip leakage losses are not only dominant near the tip but they also diffuse into the passage. Losses generated due to flow separation from the corner of the rotor hub and horseshoe vortex originating from the leading edge of the rotor blades can be seen in the light blue region near the rotor hub close to pressure side of the blade. A view of this separation vortex can be seen in Figure 8.

Figure 8 shows streamlines drawn around the fan rotor at 12000 rpm in the relative frame of reference. Streamlines are colored by velocity magnitude in the rotational frame. Complex and detailed flow features around the fan rotor blades and rotating hub can be seen from the Figure. Low momentum fluid near the rotor hub is separated from the corner of the hub and rolled up into a vortical structure. This vortical structure may combine with other three dimensional and recirculatory flow system originating near the leading edge of the rotor blades. The cross flows on the endwall surface may influence the final form of the hub separation region.

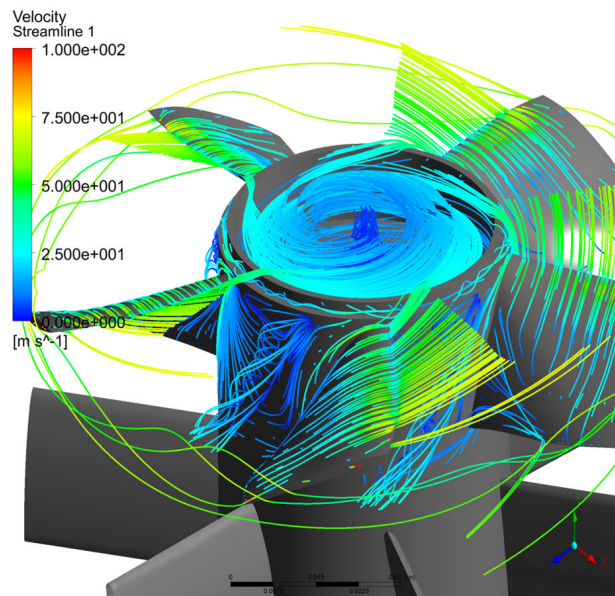


Figure 8: **Computationally obtained streamlines near the ducted fan at 12000 rpm, in the relative frame of reference**

### **EFFECT OF ROTOR HUB SHAPE**

Separation from the corner of the rotating hub is a significant source of loss for the current 127 mm diameter fan rotor. It is noted that this separation effect is highly dependent on the rotor hub geometry. During our initial calculations, a rotor hub without a cavity near the center was modeled as shown in Figure 9a. Figure 9 shows streamlines drawn around these rotor hub configurations. It can be concluded from Figure 9a that flow impinging on the rotor hub without a cavity has strong radial components. Because of this radial flow near the sharp corner of the rotor blade, it is hard to turn the flow near the hub region of the rotor blade. Because of increasing adverse pressure gradient on the junction of rotor blade leading edge and rotor hub, a vortical structure originates from the junction point and increases the strength of hub separation and losses from the hub. However a cavity on the center of the rotor hub as shown in Figure 9b and step on the corner makes smooth transition for the flow from the rotor hub to the rotor blade. It also reduced the losses related to hub separation. Figure 7 shows the results with a cavity near the center of rotation.

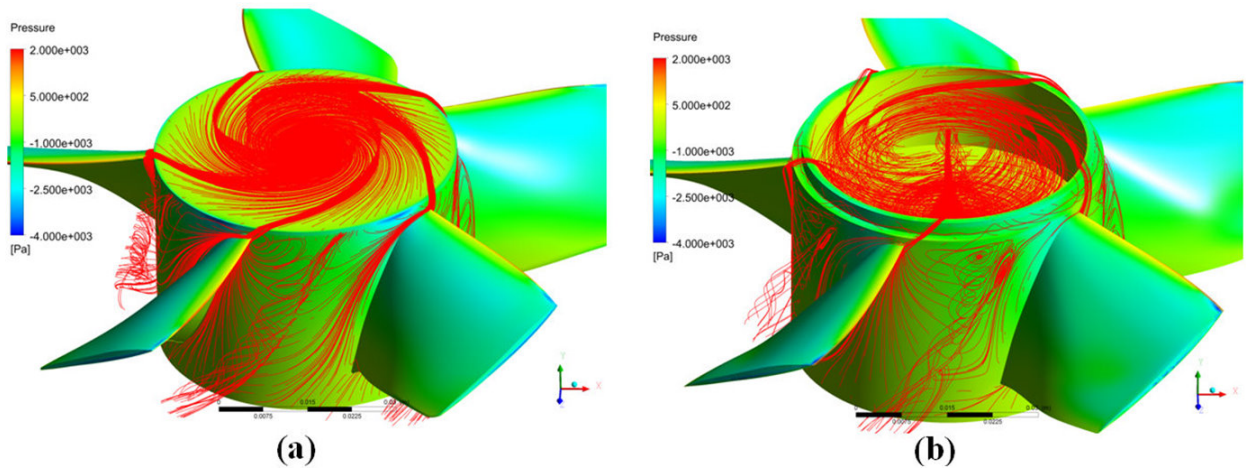


Figure 9: **Streamlines drawn around fan rotor hub for two different configurations (a) rotor hub without a cavity on center and step on corner (b) rotor hub with a cavity on center and step on corner**

## CONCLUSIONS

In this paper, a computational investigation around a ducted fan for VTOL UAV applications was carried out. Computational method that involves full rotor simulations was used for hover performance predictions of ducted fans.

Total pressure computational predictions of mean flow at the fan rotor exit are in very good agreement with the experimental measurements except the regions near the rotor hub.

Disk loading computations were also in a good agreement with experimental measurements especially for low rotational speeds.

Fan rotor exit relative total pressure contour was drawn for a fixed position of rotor blades. Main sources of loss for a ducted fan fan rotor were tip leakage related losses, rotor wake losses and hub region related losses.

Separation from the corner of the rotating hub is a significant source of loss for our 127 mm diameter fan rotor. It is noted that this separation effect is highly dependent on the rotor hub geometry.

Because of the strong radial components that are generated by the flow impinging on the rotor hub without a cavity, it is hard to turn the flow near the hub region of the rotor blade. A vortical structure originates from the junction point and increases the strength of hub separation and losses from the hub.

A cavity on the center of the rotor hub as shown in Figure 9b and step on the corner makes smooth transition for the flow from the rotor hub to the rotor blade.

## REFERENCES

- Abrego, A. I. and Bulaga, R. W. (2002). Performance study of a ducted fan system. *AHS Aerodynamics, Aeroacoustic , Test and Evaluation Technical Specialist Meeting*.
- Ahn, J. and Lee, K. T. (2004). Performance prediction and design of a ducted fan system. *40th AIAA/ASME/SAE/ASEE Joint Propulsion Conference and Exhibit*.
- Akturk, A. and Camci, C. (2009). Piv measurements and computational study around 5-inch ducted fan v/stol uav. *47th AIAA Aerospace Sciences Meeting and Exhibit*, (AIAA-2009-332).
- Akturk, A. and Camci, C. (2010). Influence of tip clearance and inlet flow distortion on ducted fan performance in vtol uavs. *6th AHS Forum*, (AHS 2010-338).
- ANSYS (2009a). Ansys-cfx solver modeling guide.

ANSYS (2009b). Ansys-cfx solver theory guide.

Chang, I. C. and Rajagopalan, R. G. (2003). Cfd analysis for ducted fans with validation. *21th AIAA Applied Aerodynamics Conference*.

Fleming, J., Jones, T., Lusardi, J., Gelhausen, P., and Enns, D. (2004). Improved control of ducted fan vtol uavs in crosswind turbulence. *AHS 4th Decennial Specialist's Conference on Aeromechanics*.

Graf, W., Fleming, J., and Wing, N. (2008). Improving ducted fan uav aerodynamics in forward flight. *46th AIAA Aerospace Sciences Meeting and Exhibit*.

He, C. and Xin, H. (2006). An unsteady ducted fan model for rotorcraft flight simulation. *62th AHS Forum*.

Ko, A., Ohanian, O. J., and Gelhausen, P. (2007). Ducted fan uav modeling and simulation in preliminary design. *AIAA Modeling and Simulation Technologies Conference and Exhibit*.

Lind, R., Nathman, J. K., and Gilchrist, I. (2006). Ducted rotor performance calculations and comparisons with experimental data. *44th AIAA Aerospace Sciences Meeting and Exhibit*.

Martin, P. and Tung, C. (2004). Performance and flowfield measurements on a 10-inch ducted rotor vtol uav. *60th Annual Forum of the American Helicopter Society*.

Mort, K. W. and Gamse, B. (1967). A wind tunnel investigation of a 7-foot-diameter ducted propeller. Technical Report NASA TND-4142.

Mort, K. W. and Yaggy, P. F. (1962). Aerodynamic characteristics of a 4-foot-diameter ducted fan mounted on the tip of a semispan wing. Technical Report NASA TND-1301.

Wilcox, D. C. (1993). *Turbulence modeling for CFD*. La Caada: DCW Industries, Canada.

Yaggy, P. F. and Mort, K. W. (1961). A wind-tunnel investigation of a 4-foot-diameter ducted fan mounted on the tip of a semispan wing. Technical Report NASA TND-776.

Zhao, H. W. and Bil, C. (2008). Aerodynamic design and analysis of a vtol ducted-fan uav. *26th AIAA Applied Aerodynamics Conference*.